A&A 490, 1–14 (2008)
DOI: 10.1051/0004-6361:200810092

Astronomy & Astrophysics

OTELO survey: deep *BVRI* broad-band photometry of the Groth strip

I. Number counts and two-point correlation functions⋆

J. Cepa[1,2], A. M. Pérez-García[1], A. Bongiovanni[1], E. J. Alfaro[3], H. Castañeda[1], J. Gallego[4], J. I. González-Serrano[5], M. Sánchez-Portal[6], and J. J. González[7]

[1] Instituto de Astrofísica de Canarias, 38205 La Laguna, Spain
e-mail: jcn@iac.es
[2] Departamento de Astrofísica, Universidad de La Laguna, Spain
[3] Instituto de Astrofísica de Andalucía-CSIC, Granada, Spain
[4] Departamento de Astrofísica y CC. de la Atmósfera Universidad Complutense de Madrid, Madrid, Spain
[5] Instituto de Física de Cantabria, Santander, Spain
[6] Herschel Science Center, INSA/ESAC, Madrid, Spain
[7] Instituto de Astronomía UNAM, México D.F, México

Received 29 April 2008 / Accepted 8 July 2008

ABSTRACT

Context. The Groth field is one of the sky regions that will be targeted by the OTELO (OSIRIS Tunable Filter Emission Line Object) survey in the optical 820 nm and 920 nm atmospheric windows. A complementary broad-band photometric catalogue of the field is essential for several purposes, in particular the inequivocal identification of sources, photometric redshift estimation, and population synthesis fitting.
Aims. We aim to describe the OTELO survey and present deep *BVRI* imaging data of the Groth field. Galaxy number counts, colour distributions and galaxy clustering are analysed.
Methods. *BVRI* deep images (>8 ks) were obtained with the Prime Focus Camera at the WHT (La Palma) and reduced with the IRAF package. The extraction and photometry of the sources was done with SExtractor software. We analysed the final catalogue to obtain galaxy number counts, as well as galaxy correlation functions as a function of I magnitude and $V - I$ colour. It is also compared with estimations from mock catalogues of the Virgo-Millenium consortium.
Results. We find excellent agreement between observed and mock data number counts. We also find evidence of galaxy clustering evolution and strong dependence of the angular correlation function on the observed $V - I$ colour. Our data favour a flattening of the clustering amplitude with median apparent magnitude. The good general agreement between our clustering analysis and the estimates from the mock data is remarkable.

Key words. galaxies: evolution – galaxies: statistics – large-scale structure of Universe

1. Introduction

Extragalactic surveys are extremely useful and necessary tools for studying the cosmic evolution of galaxies. On the one hand, pencil-beam surveys can be deep enough to properly study the luminosity and morphology evolution, but they cover relatively small sky areas and may suffer from field-to-field variance. On the other hand, wider surveys are limited to being shallower, but provide the complementary study of the local large-scale structure and establish the local baseline against which to contrast the evolution of the more distant galaxy populations detected in deeper surveys.

Broad-band multicolour photometry allows observation of the faintest targets. With an appropriate band selection for adequate spectral sampling, a redshift estimation, commonly known as photo-z, can be obtained with tools such as Hyper-z (Bolzonella et al. 2000) or BPZ (Benítez 2000). These imaging surveys also permit morphological classification of all sufficiently resolved sources, with techniques that analyze the light distribution either directly (GIM2D tool, Simard et al. 2002) or through multi-parametric fits (GALFIT tool, Peng et al. 2002). Spectroscopic follow-up is needed afterwards to provide precise redshifts, more detailed spectral energy distributions; and valuable information on the stellar populations, chemical evolution, star formation rates (SFR), and even dynamical masses of the photometrically selected targets.

Examples of deep imaging surveys are the now classical Hubble Deep Field North and South (Williams et al. 1996, 1998), while examples of spectroscopic surveys are VVDS (Le Fèvre et al. 2005), DEEP, and DEEP2 (Koo et al. 2005; Davis et al. 2000, respectively). Among surveys that cover large areas either in multicolour photometry or in spectroscopy are 2dF (Colless et al. 2001), SDSS (York et al. 2000), Combo-17 (Wolf et al. 2003), and Alhambra (Moles et al. 2007).

Deep imaging programmes have been performed as preparatory work to support future complex surveys, such as several

⋆ Based on observations obtained at the 4.2 m WHT telescope operated on the island of La Palma by the Isaac Newton Group of Telescopes in the Spanish Observatorio del Roque de Los Muchachos of the Instituto de Astrofísica de Canarias.

VLT surveys for GOODS, COSMOS, and VVDS. Likewise, this paper presents a deep *BVRI* broad-band survey in one of the fields of the Groth strip selected for the OTELO survey (OSIRIS Tunable Emission Line Object survey), a uniquely deep and complete narrow-band survey for emission objects to be carried out with the 10.4 m GTC telescope, as described in the next section of this paper.

The galaxy correlation function derived from wide-area surveys has shown that the clustering observed at angular scales of about a degree is luminosity dependent (see for example Zehavi et al. 2002; Norberg et al. 2002). On scales of a few arcminutes, the correlation function provides important constraints for the spatial distribution and occupation number of dark matter haloes, a key piece of information to fine-tune hierarchical structure formation theory and the broad spectrum of related simulations. Our work here presents this analysis as applied exclusively to the Groth-Westphal field.

The OTELO project is described next in this paper followed by a section on the observation and data reduction processes of its preparatory broad-band survey. The detection efficiency, number counts, and colour distribution of the sample are presented next, concluding with the analysis and discussion of the angular correlation function estimations.

2. The OTELO project

OSIRIS (optical system for imaging and low-resolution integrated spectroscopy) (Cepa et al. 2003, 2005a) is the Day One instrument of the GTC 10.4 m telescope for the optical wavelength range. It is a general-purpose instrument for imaging and low-resolution, long-slit, and multi-object spectroscopy (MOS). OSIRIS has a field of view of 8.6 × 8.6 arcmin, which makes it ideal for deep surveys, and it operates from 365 through 1000 nm. The main characteristic that makes OSIRIS unique among other instruments in 8–10 m class telescopes is the use of tunable filters (TF) (e.g. Bland-Hawthorn & Jones 1998). These allow a continuous selection of both the central wavelength and the bandwidth, thus providing scanning narrow-band imaging within the OSIRIS wavelength range. The combination of the large GTC aperture, large OSIRIS field of view, and availability of the TFs will allow a truly unique emission line survey: OTELO (Cepa et al. 2005b, 2007).

2.1. Scientific strategy

OTELO will scan the wavelength intervals, or windows through the OH emission line forest, centred at 815 and 920 nm, with spectral windows of 15 and 18 nm, respectively. Telluric bands in the first window are insignificant, while their higher strength around 920 nm and CCD quantum efficiency drop will require an increase in the exposure time of ≃15% (Stevenson 1994) in this window. This technique provides datacubes that are equivalent to 3D low-resolution spectroscopy for the targeted emission lines.

The total area to be covered with OTELO is 0.1 square degrees, distributed on the fields GOODS–N, GROTH, SXDS, and selected areas of ACS/COSMOS, to control cosmic statistics. The estimated total exposure time is about 20 dark nights with ≃1 arcsec seeing. As shown in Table 1, a wide range of redshifts will be surveyed at each OTELO window depending on the emission line detected. The resolution and sampling will be such that the [NII]λ658.4 nm line can be accurately deblended from Hα, which is essential for SFR and metallicity determination. Table 2 summarises the main characteristics of OTELO survey.

Table 1. Central redshifts to be observed in both OTELO windows for some significant emission lines.

Line	z@815 nm	z@920 nm
Hα	0.24	0.40
OIIIλ500.7 nm	0.63	0.84
OIIλ372.7 nm	1.19	1.47
CIVλ154.9 nm	4.26	4.94
Lyα	5.70	6.57

To achieve the maximum scientific explotation of OTELO, a cross correlation is required with the broad-band *UBVRIJK* auxiliary survey currently under way for the same fields. This survey, whose initial results are presented in the present paper, complement OTELO by allowing identification of the emission-line detected via photometric redshifts, and whenever possible, a morphological classification of the objects.

The expected follow-ups include optical and near-infrared (NIR) MOS and far-infrared (FIR) observations. A fraction of the targets at $0.6 < z < 1.5$, i.e. those with Hα in the NIR domain and [OII]λ372.7 nm, [OIII]λ500.7 nm in the OTELO spectral windows, will be observed with NIR spectrographs to determine Hα and [NII] fluxes for SFR calculations and metallicity determinations. In the FIR, cross-correlation with 60–600 μm images of some OTELO fields obtained with PACS and SPIRE instruments on board Herschel observatory (Pilbratt 2005) using guaranteed time will allow obtaining complete SEDs to derive-extinction corrected SFRs and FIR properties of the different sources detected with respect to cosmic time.

2.2. OTELO in the context of other extragalactic surveys

The past few years of research in the field of faint galaxies have been dominated by the long-term spectroscopic surveys carried out with 8 m-class telescopes. These surveys, for example DEEP and DEEP-2 (Koo et al. 2005; Davis et al. 2000, respectively) with DEIMOS at the Keck or VVDS (Le Fèvre et al. 2005) with VIMOS at the VLT, have in common that the sample selection has been done by apparent magnitude limit in one or at most two optical broad bands.

OTELO will be a long-term survey with an unprecedent limiting emission-line flux detection ($\approx 1 \times 10^{-18}$ erg s^{-1} cm^{-2}). OTELO will therefore introduce unexplored parameters in the large-scale survey space. The feasibility of such an approach has been demonstrated by, for example, Jones et al. (2002) with the AAO 4 m telescope, and Hippelein et al. (2003) with the CAHA 3.5 m telescope. However, OTELO will be unique, because it will be the first large-scale emission-line survey fully exploiting the sensitivity and the spectral resolution of tunable filters in a 10 m telescope (Table 2).

2.3. Scientific aims

A deep general-purpose survey such as OTELO provides very valuable data for tackling a wide variety of projects. Science cases where OTELO will likely have the greatest impact include: SFR density evolution in the Universe, Lyα emitters (González–Serrano et al. 2005a), high-redshift QSO (González–Serrano et al. 2005b), AGNs at any redshift (Sánchez-Portal et al. 2005), chemical evolution of the Universe up to $z = 1.5$ (Cepa et al. 2005b), emission line ellipticals, and galactic emission stars (Alfaro et al. 2003). The total number of emission-line galaxies and its distribution within the

Table 2. Main characteristics of OTELO survey.

Depth	*EW*	Area	Comments
10^{-18} erg cm^{-2} s^{-1}	≤3 nm	0.1 sq. deg.	[NII]λ658.4 nm/Hα deblending

Table 3. Log of observations (coordinates refer to J2000.0).

Field	RA	Dec	Filter	Exposure time (s)	Seeing (arcsec)	Date
1	14:16:35.0	52:16:25	*B*	9000(9 × 1000)	1.1	May 2004
			V	9000(9 × 1000)	0.9	May 2003; May 2004
			R	9000(10 × 900)	1.0	May 2003; May 2004
			I	11 000(10 × 800; 5 × 600)	0.9	May 2003; May 2004
2	14:17:36.2	52:28:04	B	9000(9 × 1000)	1.0	May 2003; May 2004
			V	9000(9 × 1000)	0.9	May 2004
			R	9000(10 × 900)	0.9	June 2003
			I	9000(15 × 600)	1.0	June 2003; May 2004
3	14:15:34.8	52:04:45	*B*	9000(9 × 1000)	1.1	May 2004
			V	9000(9 × 1000)	1.2	June 2003; May 2004
			R	9000(10 × 900)	1.1	June 2003; May 2004
			I	8400(14 × 600)	1.1	June 2003; May 2004

different classes is a relevant science case on its own, given the present uncertainties in the evolution of the luminosity functions. Assuming no evolution and a cosmology with $\Omega_M = 0.3$, $\Omega_\Lambda = 0.7$, $H_0 = 65$ km s^{-1} Mpc^{-1}, the total number of emitters in OTELO survey is expected to be 4×10^4, with 77% spirals and ellipticals up to redshifts of 1.5 and 0.84, respectively, 18% Seyfert galaxies at $z \leq 1.5$, 2% blue compact dwarfs up to $z = 0.85$, 2.5% Lyα emitters at z up to 6.7 (equivalent to 10% of the age of the Universe), and about 0.5% galactic emission stars. The low-resolution spectra extracted from the data cubes will allow deblending of the Hα from the [NII]$\lambda\lambda$654.8,658.4 nm lines, thus allowing an estimation of the metal contents of the targets (Cepa et al. 2005b) and the possibility of a zero-order distinction between the various AGN types (Sánchez-Portal et al. 2005).

3. Complementary broad-band survey

OTELO requires a complementary broad-band survey for several relevant and specific purposes: to identify and characterise the morphology of the detected emission sources, to estimate a photometric redshift for an unambiguous identification of the emission line detected, to determine the true fraction of emission line objects for each morphological type, to study the environment and to make an approximate population synthesis of the sources.

Given that the closest intense emission lines that may get confused in the OTELO scans are Hβ and [OIII]λ500.7 nm, a photometric redshift accuracy of 0.03 is required in the redshift range around $z = 0.8$. According to Table 2 of Bolzonella et al. (2000), this accuracy can be achieved with *UBVRIK* or *BVRIJK* photometry with an error in magnitude lower than $\Delta m = 0.05$. The OTELO team is currently obtaining the required *UBVRIJK* deep data, some of which are presented in this paper. Very complete morphology classification will actually be possible because the fields considered also have deep HST images. Beyond morphology and photometric redshifts, the *U* or *u* filter is also a key to identifying potential QSOs, the *K* band is extremely useful for the approximated population synthesis and, in relation to the environment of the sources, the presence of a red sequence in the images will also be of use in identifying galaxy clusters.

The broad-band data gathering for the OTELO fields started in 2003, with its first results discussed next through the remaining sections of this paper. It is an ambitious effort to be continued in parallel and until the end of the actual OTELO narrow-band survey with OSIRIS at the GTC, which also expects to benefit from public data available from other collaborations.

4. The present broad-band data

4.1. Observations and reduction

The Extended Groth Strip is one of the selected fields for the OTELO project. Given its low galactic extinction, low stellar density, and the scarcity of bright objects in the field, this is a commonly observed sky region in extragalactic astronomy for studies with a broad diversity of scientific aims. A multi-wavelength coverage of this wide area is being carried out by different teams worldwide (Gould et al. 1997; Im et al. 2002; Miyaji et al. 2003; Cristóbal-Hornillos et al. 2003; Coppin et al. 2005; Nandra et al. 2005; Vogt et al. 2005; Barmby et al. 2006; Sarajedini et al. 2006; Georgakakis et al. 2006; Willner et al. 2006). Although optical broad-band photometry has been obtained by several of these groups, none is at once deep and wide enough for the OTELO purposes, hence the need for our group to carry out its own broad-band survey in selected areas of Groth.

Three different pointings within Groth were observed, covering a total area of 0.18 square degrees with the *B*, *V*, *R*, and *I* filters. Observations were carried out during several runs using the Prime Focus Camera at the 4.2 m William Herschel Telescope (WHT) of the Observatorio del Roque de los Muchachos (La Palma, Canary Islands). The camera has two adjacent CCDs (2k × 4k), covering a field of view of $16' \times 16'$ with a scale of 0.237 arcsec per pixel. To avoid high sky-background counts and cosmic ray events, several exposures of 600, 800, 900, or 1000 s were taken at each pointing. A dithering pattern with offsets of ~15 arcsec between consecutive exposures was followed in order to easily identify and remove cosmetic flaws. Table 3 summarises the exposures for each pointing and filter observed.

Data sets were first processed following standard reduction steps (bias and flat-field correction) using IRAF packages. The *R* and *I* images, in particular, suffer from the fringing caused by the multiple reflection and interference of the night sky emission lines with the CCDs. To correct this effect, all dithered *R*

Table 4. Fitted coefficients of the photometric error model $err(m) = A + e^{Cm-B}$.

Filter	A	B	C
B	0.	22.1	0.79
V	0.	23.1	0.86
R	0.	23.2	0.87
I	0.	23.7	0.91

and I target frames from a given night were median-combined, effectively clipping out sources and providing a master image that maps the fringing pattern of the sky for each band. This master fringing map was then subtracted from each image within the night, scaling it first to the fringe level observed in each target frame. The fringing amplitudes were ∼6% for the R band and ∼15% for the I band. After correction, the residual fringing effects were typically three times less (∼2% and ∼5% for the R and I bands, respectively). Flat-field images pointing to blank fields were taken during twilight.

The astrometric calibration was carried out by cross correlation with the USNO B1.0 astrometric catalogue (Monet et al. 2003), available from the International Celestial Reference System (ICRS). Each individual CCD frame was calibrated independently by fitting more than one hundred objects. The fit residuals were typically ∼0.25−0.3 arcsec RMS and showed no systematic trends with magnitude or celestial coordinate. As a double-check, the 2MASS catalogue (Skrutskie et al. 2006) was also used, yielding astrometric transformations and residuals consistent with those obtained with the USNO B1.0 catalogue.

For each filter, all fully-reduced astrometric-calibrated frames were finally coadded into final science images with total effective exposures of 9000 s in B, V, and R at all three Groth pointings, and 11 000, 9000, and 8400 s in the I filter at the first, second, and third pointings respectively (see Table 3).

4.2. Instrumental magnitudes

Instrumental magnitudes were measured using the source detection and light-profile analysis algorithm SExtractor v2.4 (Bertin & Arnouts 1996). Source detection in SExtractor depends on two fundamental parameters, minimum area and detection threshold. We adopted a minimum detection area of 15 pixels (∼seeing disc) and a detection threshold 1.5σ above the local background. This threshold implies the reasonable signal-to-noise ratio of $SNR = 5$ in the detection (Harris 1990). For each detection, SExtractor then calculates aperture, isophotal, and Petrosian magnitudes and provides a quantitative indicator of whether the detection is a point or an extended source. For stellar type objects (point sources), the aperture magnitude is the most appropriate. After a careful comparison of fluxes obtained with different apertures in all five bands, an aperture of 22 pixels (5.2 arcsec) was determined to be the optimal one to be used in all *BVRI* science images. The increase with magnitude of the internal photometric errors is actually quite well characterised by a simple exponential function, $err(m) = A + e^{Cm-B}$ (see Fig. 1). The coefficients of the exponential function fitted to the errors of each band are summarised in Table 4.

4.3. Photometric calibration

A proper photometric calibration can be derived comparing our stellar catalogue (objects with SExtractor `star-class` parameter >0.9 in all four *BVRI* bands) with the Sloan Digital Sky Survey (SDSS). All common stars, with g, r, and i band photometric errors below 0.05 in the SDSS catalogue (DR4), were selected for our calibration purposes.

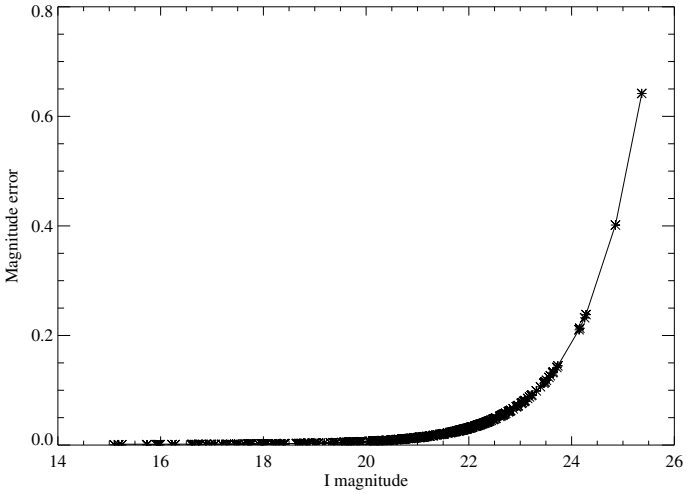

Fig. 1. Sextractor internal photometric errors for I magnitude. Continuous line is the exponential fitting to the data.

The Lupton (2005) equations[1] were taken among the different transformations between Sloan and Johnson stellar magnitudes (Vega system):

$$B = g + 0.3130(g - r) + 0.2271;\ \sigma = 0.0107 \quad (1)$$

$$V = g - 0.5784(g - r) - 0.0038;\ \sigma = 0.0054 \quad (2)$$

$$R = r - 0.2936(r - i) - 0.1439;\ \sigma = 0.0072 \quad (3)$$

$$I = r - 1.2444(r - i) - 0.3820;\ \sigma = 0.0078. \quad (4)$$

Median differences in V, $B - V$, $V - R$ and $V - I$ between our instrumental and the SDSS transformed magnitude and colours were first computed with a whole calibrating stellar sample (typically 45 to 65 stars in each of our pointings). After rejecting those stars that deviated more than 2σ from the median differences, the process was iterated to adopt the final photometric calibration summarised in Table 5.

To guarantee that the stellar photometric calibration is sturdy enough to provide consistent results for normal galaxies, the above procedure was also run for testing other alternative transformations between the SDSS and the Johnson photometric systems (Jester et al. 2005). In all cases, the derived zero points were consistent with those obtained through the Lupton transformation but showed typically higher RMS dispersions.

4.4. Source catalogue and detection efficiency

After applying the above photometric calibrations for each detector and pointing, the final catalogue was built by crossing the individual detections among filters and pointings, within a tolerance of 0.7 arcsec. Our grand source catalogue has ∼44 000 objects.

To determine the detection efficiency, artificial point sources were added to the science images, in random coordinates and with the same FWHM of the real point sources in the frame. To recover these objects, SExtractor was used again under the same criteria as before. The detection efficiency so derived depends somewhat on the FWHM (seeing). Limiting magnitudes,

[1] Available in `http://www.sdss.org`

Table 5. Zero points of photometric calibration with their typical and mean deviations.

Field	V			$B-V$			$V-R$			$V-I$		
	V_0	σ	$\langle\sigma\rangle$	$(B-V)_0$	σ	$\langle\sigma\rangle$	$(V-R)_0$	σ	$\langle\sigma\rangle$	$(V-I)_0$	σ	$\langle\sigma\rangle$
1 (CCD1)	0.96	0.02	0.01	–0.18	0.06	0.05	0.0	0.02	0.01	0.66	0.07	0.06
1 (CCD2)	0.97	0.01	0.01	–0.08	0.07	0.06	–0.06	0.02	0.02	0.55	0.03	0.03
2 (CCD1)	0.92	0.03	0.02	–0.19	0.05	0.04	0.03	0.06	0.04	0.63	0.04	0.03
2 (CCD2)	0.96	0.03	0.02	–0.11	0.06	0.05	0.05	0.02	0.02	0.61	0.05	0.04
3 (CCD1)	0.87	0.03	0.02	–0.10	0.05	0.04	–0.08	0.02	0.02	0.64	0.05	0.04
3 (CCD2)	0.91	0.02	0.02	0.01	0.03	0.03	–0.07	0.02	0.02	0.58	0.04	0.04

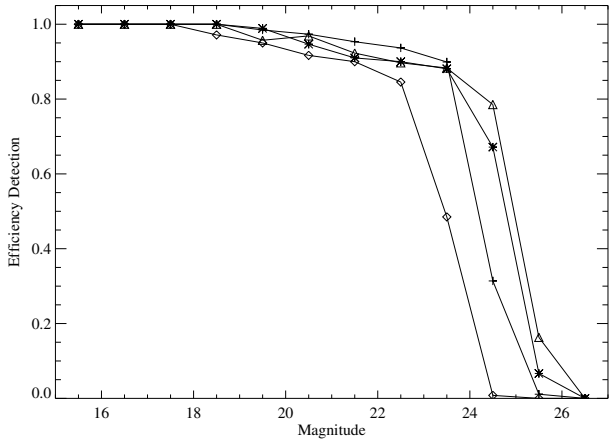

Fig. 2. Detection efficiency for the Groth1 field. *B* (triangles), *V* (asterisks), *R* (crosses) and *I* (diamonds) filters are shown. In all cases, magnitude is instrumental.

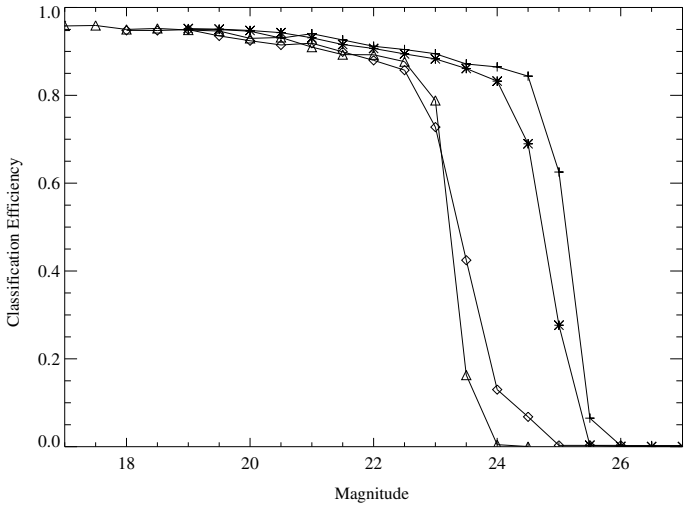

Fig. 3. Point-source discrimination efficiency in the *B* (crosses), *V* (stars), *R* (diamonds), and *I* (triangles) filters.

defined as the magnitude at 50% detection efficiency, are 25.0, 25.0, 24.5, and 23.5 for the *B*, *V*, *R*, and *I* bands, respectively (Fig. 2).

Source confusion makes the detection efficiency worse, but its effects are difficult to parametrize and quantify. To gauge the source confusion effects, artificial point sources were added not randomly but now far enough from the catalogue and previously positioned artificial sources. After comparing both experiments, it is found that source confusion effects are negligible (∼4% of the objects in brighter magnitudes and ∼7% in weaker objects are lost). Consequently, the source confusion effect on the detection efficiency in *B*, *V*, and *R* bands may result in a negligible decrease in 0.05 in the limiting magnitude, while it reaches 0.2 mag in the case of the I band.

4.5. Spurious detections

The test proposed by Saracco et al. (1999) was performed to evaluate the number of spurious sources and their magnitude distribution. The test assumes that noise of all frequencies is symmetrical with respect to the mean sky value. For each filter, a noise frame was created combining all unregistered frames. This noise frame has a similar background level and patterns as the actual data. Reversing this noise frame, the negative fluctuations are revealed and the residual of the real sources are made negative (and undetectable). Spurious detections are now quantified running SExtractor in the reversed image, with the same parameters used in the science images. In this fashion, the spurious contamination was found to be a negligible fraction of the detected sources (∼1% in the most extreme case in the whole sample).

4.6. Star-galaxy distinction

Looking at the peak intensity and the isophotal area of each detected source for a given seeing, the SExtractor program reports a galaxy/star classifier parameter, varying from zero for a galaxy-like extended source to unity for a point-source or stellar-like unresolved object. The SExtractor point-source discriminator works quite well at bright magnitudes, but its efficiency naturally decreases at lower signal-to-noise ratios and with increasing width or deterioration of the point spread function. Intermediate values of the `star-class` parameter are indicative of the discrimination uncertainties. In this work, only objects with `star-class` parameter above 0.9 were considered bona-fide stars. To test the validity of this somewhat arbitrary threshold, the SExtractor algorithm was applied to images with simulated point sources mimicking the magnitude range and noise characteristics of the actual science images. The results, shown in Fig. 3, indicate that significant discrimination errors do not appear until a 24.5 mag in the *B* and *V* and at 23 mag in the *R* and *I* filters. Since the fraction of stars at these and fainter magnitudes is expected to become absolutely negligible, it is clear that the adopted threshold, and the SExtractor stellar discrimination algorithm itself, work quite effectively for the purposes of the present study.

5. Galaxy number counts

Accurate galaxy number counts in specific bands provide strong constraints on galaxy evolution (Tinsley 1980). Detection of faint galaxies has significantly improved through the increasing number and quality of recent surveys. Previous to the present

Table 6. Slope of differential number counts.

Filter	Our data	Metcalfe (2001)	Capak (2004)	McCracken (2004)	Eliche (2006)
B	0.458(±0.01)	0.25	0.45	0.45	0.497
V	0.382(±0.01)		0.40	0.40	
R	0.331(±0.01)	0.37	0.36	0.37	
I	0.337(±0.01)	0.33	0.33	0.34	

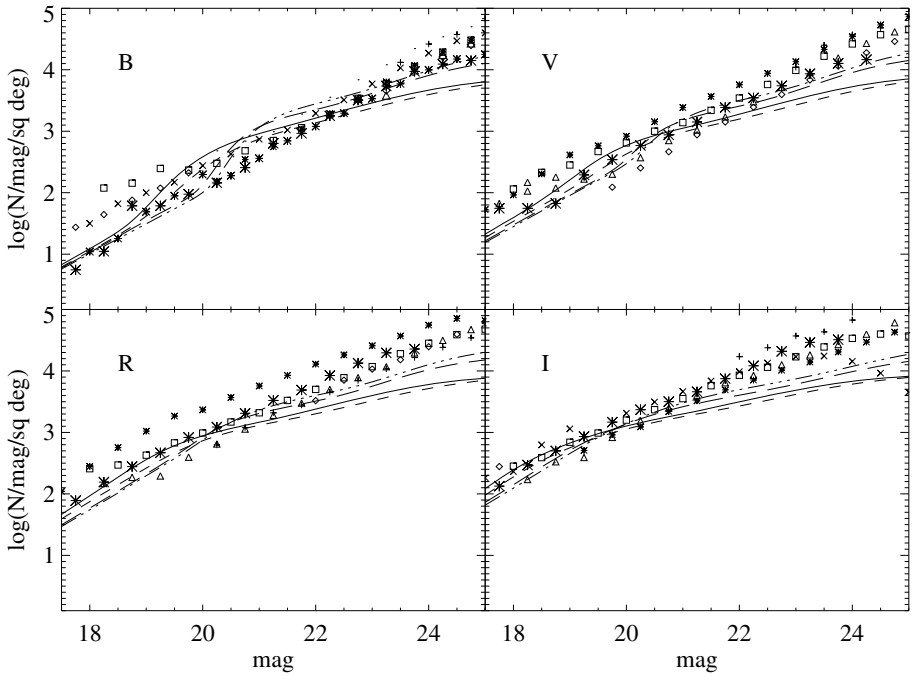

Fig. 4. Differential number counts (small asterisks) from the present WHT data in the *B*, *V*, *R*, and *I* bands. Independent results from the literature are also shown for comparison: Arnouts et al. (1999) (large asterisks), Capak et al. (2004) (crosses), Eliche-Moral et al. (2006) (points), Gardner et al. (1996) (diamonds), Jones (1991) (triangles), Kashikawa et al. (2004) (squares), McCracken et al. (2003) (X-crosses), MacDonald et al. (2004) (big crosses), Metcalfe et al. (1995) (big diamonds), and Metcalfe et al. (2001) (big triangles). Lines present predictions from a set of modified Gardner models: number evolution of Rocca-Volmerange & Guiderdoni (1990) with $\tau = 0.2$ (continuum line) or $\tau = 0.6$ (dashed line) extinction law, number evolution of Broadhurst et al. (1992) with $\tau = 0.6$, and merger rate $Q = 1$ (long dashed line) or $Q = 1.6$ (three point-dashed line). See text for details.

auxiliary OTELO survey, the vast majority of surveys either cover large areas with a shallow depth (Yasuda et al. 2001) or are deeper over very limited areas (Metcalfe et al. 2001). Nonetheless, the Capak et al. (2004) dataset is comparable to the one in this work in both area and depth, while the McCracken et al. (2007) data is actually deeper and covers an even larger area. In this section, our galaxy number counts are contrasted with model predictions and with several observational studies, in particular with the work of Eliche-Moral et al. (2006) who analysed a *U*, *B*, and *K*-bands galaxy census for the same Groth field.

Differential galaxy number counts (per square degree per half magnitude) in the *B*, *V*, *R*, and *I* bands are shown in Fig. 4 and listed in Table 6, as derived from the `AUTO` magnitudes of all extended sources in our catalogue. These "raw" counts, with no incompleteness corrections applied, are in good agreement with previous studies (Metcalfe et al. 1995; Gardner et al. 1996; Arnouts et al. 1999; Metcalfe et al. 2001; McCracken et al. 2003; Capak et al. 2004; Kashikawa et al. 2004; MacDonald et al. 2004; Eliche-Moral et al. 2006), as shown in Fig. 4.

The slope of the observed number count distribution (as derived from least-squares fits in the 19 to 23 mag range) $\mathrm{d}\log(N)/\mathrm{d}\log(m)$ was found to be 0.46, 0.38, 0.33, and 0.34 for *B*, *V*, *R*, and *I*, respectively, with an error of ≃0.01 in all bands. Lilly et al. (1991) claim a change in slope for the *B* number counts at $B = 25$ that does not shows in our data, but a flattening at magnitudes fainter than $B = 24$ ($\mathrm{d}\log(N)/\mathrm{d}\log(m) = 0.34 \pm 0.004$), similar to what is found by McCracken et al. (2003) and Metcalfe et al. (1995), is clearly present.

The predicted number of galaxies with a given apparent magnitude depends on the local space density, the assumed cosmology, and on several functions that determine the redshift distribution for each galaxy type and magnitude, such as the galaxy luminosity function, the star formation history, evolution of dust and formation epochs, among others. We compared our number counts with models of Gardner (1998). These models predict number counts including the galaxy spectral energy distribution (SED) and allow the inclusion of any number of spectral types. Theoretical SEDs come from population synthesis models and galaxy isochrone synthesis spectral evolution (Bruzual & Charlot 1993). Any star formation history is possible and the effects of metallicity are also included. Free parameters include the luminosity function, cosmological geometry and the effects of dust and merging. We used the standard cosmological model ($q_0 = 0.5$, $H_0 = 65$) and the local luminosity function of Nakamura et al. (2003). This luminosity function has morphological dependence and has been obtained from SDSS data (York et al. 2000) with the r^* filter. Morphological types selected in our models are ellipticals, early-type spirals, late-type spirals, and irregulars, also following Nakamura's classification. For each galaxy type, star formation is parametrized by the redshift of galaxy formation (z_f) and the timescale of the decay of SFR. We adopted the same parameters for galaxy types as Eliche-Moral et al. (2006), i.e., a Salpeter IMF for all classes, solar metallicities for the E-S0 and S0-a/Sb, 2/5, and 1/5 of solar metallicity for Scd/sd, and Im groups, respectively, instantaneous star formation for E-S0, exponential for spirals types, and constant for Im galaxies (see Eliche-Moral et al. 2006, for more details).

For all galaxies, internal absorption by dust was assumed. The extinction law adopted is a power-law $\propto\lambda^{-2}$, and we assumed an extinction for the galaxies $\tau_{4500} = 0.2(L_z/L^*)^{0.5}$ at 450 nm. The coefficient for this law is 0.2, the same coefficient as

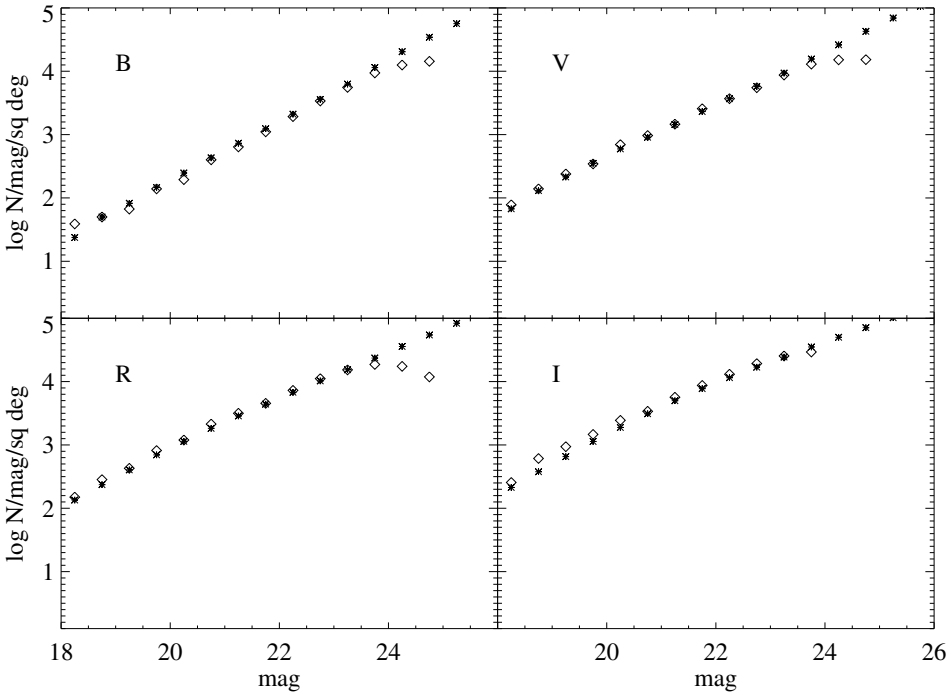

Fig. 5. Differential number counts from WHT data in *B*, *V*, *R*, and *I* filters (diamonds) and the values obtained from the mock catalogues of Kitzbichler & White (2007).

used by Gardner in the original model. We also used a modified code with this coefficient as 0.6, a value intermediate between those obtained from observations of local disc galaxies (Peletier & Willner 1992; Bosselli & Gavazzi 1994; Xilouris et al. 1999) and the Gardner value.

To model the evolution of galaxies, we considered two different functional forms (both included in Gardner's original model) for the number evolution. The first one is $\phi^* \propto (1+z)^{\beta}$, where β is the free parameter (Rocca-Volmerange & Guiderdoni 1990). The second one is the function proposed by Broadhurst et al. (1992), given by $\phi^* \propto \exp[-Q/\beta((1+z)^{-\beta}-1)]$, where Q defines the merger rate and β is a function of the look-back time.

Results of the model with different parameter values are shown in Fig. 4. As can be seen in the figure, no model can fit the observed number counts, i.e., the purely analytical models are not efficient in reproducing our observations.

For this reason, we also considered the model of Kitzbichler & White (2007). This model uses the Millenium dark matter simulation (Springer et al. 1997; Lemson et al. 2006), which follows the hierarchical growth of dark matter structures from redshift $z = 127$ to the present. Cosmology concordance ΛCDM is assumed ($\Omega_m = \Omega_{dm}+\Omega_b = 0.25$, $\Omega_b = 0.045$, $h = 0.73$, $\Omega_\Lambda = 0.75$). The final data structure is a detailed formation tree for each object present at the final time. Galaxy formation semi-analytical modelling is then carried out. This model includes gas cooling, star formation, chemical, and hydrodynamic feedback from supernovae, stellar population synthesis, and growth of supermassive black holes by accretion and mergers (see De Lucia et al. 2004, and references therein). Finally, the model used for dust treatment is based on the HI column density in the galaxy disc, and a scaling of dust-to-gas ratio (using a chemical evolution model).

With this model, we obtained a simulated set of galaxies with known intrinsic properties and observational properties that can be calculated. We applied the same conversions and selection effects to this sample as the real data. From these mock catalogues, we extracted 9 samples of galaxies with angular coverage corrected to our observed fields. From the mock catalogues we used the observer frame apparent magnitude (*AB*) in the bands available. The *AB* magnitudes were converted to the one established in this work using the expressions given in Frei & Gunn (1994). Finally, we averaged differential number counts for the 9 samples and compared with our estimations as shown in Fig. 5. It is obvious that there is excellent agreement between the model and the observations in all bands.

6. Colour distribution

Hereafter, we adopted the `AUTO` magnitude from SExtractor (Bertin & Arnouts 1996) as the closest approximation to galaxy total magnitude, which is calculated using a flexible Kron elliptical aperture (Kron 1980). *V* and *I*-band `AUTO` magnitudes for galaxies were corrected by lost flux using $m_{measured} - m_{true} = 0.06$ mag as is suggested in Bertin & Arnouts (1996). The colour indexes were established using a ∼5.2 arcsec (22 pixels) photometric aperture.

In this section we focus on 3 photometric bands of our general catalogue to represent the general behavior of colours and apparent brightness. Figure 6 shows the *BV* and *VI* colour-magnitude diagrams. At least in the case of the $V-I$ versus I diagram, the general trend represented is very close to the results given by McCracken et al. (2001) and Cabanac et al. (2000), both related with the study of faint galaxy clustering.

Because the peak of brightness distributions in each observed field is between $I = 24.05$ and 24.22, and following Cabanac et al. (2000), we have defined $I = 24$ as the limit which ensures the completeness needed for the work that follows. Analogously, we have estimated $V_{complete} = 25.5$. The vertical lines in Fig. 6 represent these values.

Figure 7 shows the $B-V$ and $V-I$ colour distributions of the complete sample for different limiting magnitudes in the *V* and *I* bands, respectively. The median of the distributions for $V < 25.5$ and $I < 24$ is 0.64 for $B-V$ and 1.42 for $V-I$, respectively.

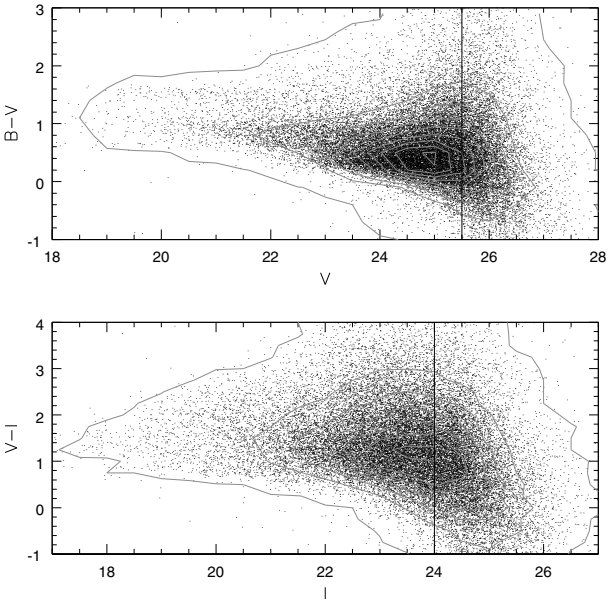

Fig. 6. Colour–magnitude diagrams for the total sample. The vertical lines indicate the completeness limits established: $V = 25.5$ and $I = 24.0$. The step of density isocontours (in galaxies per rectangular cell of 0.5×0.3 mag^2) is 150, starting from 5.

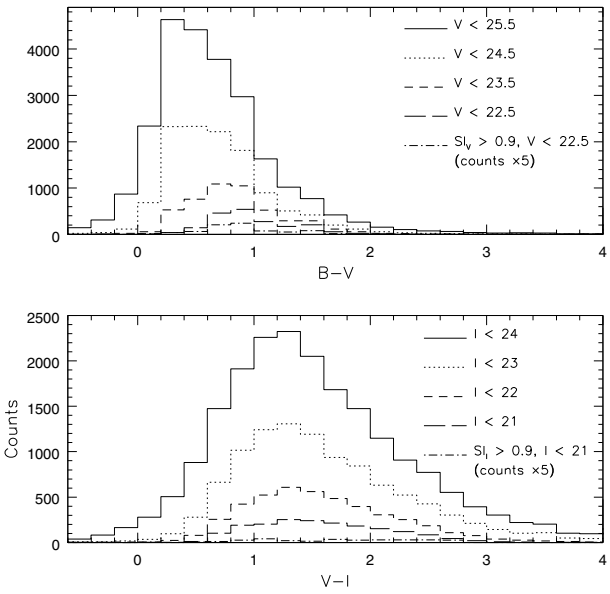

Fig. 7. Galaxy and star distributions in $B - V$ and $V - I$ colours. Star counts are multiplied by a factor 5. V and I limits are given in the legend and the faintest values correspond to the completeness limits shown in Fig. 6.

7. Angular correlation function estimation

Correlation function analysis is a standard formalism broadly used to quantify the clustering on any spatial scale. In the case of galaxies, a measure of the clustering provides clues about the underlying cosmology as well as several constraints for theories of structure formation and their evolution. The photometric data of our survey bring us an opportunity to test (via 2-point angular correlation functions or, hereafter, 2p-ACF) some recent realizations of semi-analytic models for galaxy formation on small angular scales, controlling observational parameters (apparent brightness and colour). At present, such models have taken shape in terms of simulated catalogues provided by different groups. Our specific choice of the model is described in Sect. 7.4.

The 2p-ACF defined by $\omega(\theta)$ was calculated separately for the three fields (i.e., each one is assumed to be an independent process for galaxy distribution). We selected in each field all galaxies brighter than $I = 24$ (the *complete* sample), and the 2p-ACF measurements are distributed into six non-independent I magnitude ranges ($21.5 < I_{\rm lim} < 24$; $\Delta I = 0.5$) and 14 disjointed intervals in $V - I$ colour [$-0.25 < V - I < 3.25$; $\Delta(V - I) = 0.25$]. In both cases, all objects brighter than $I = 17.0$ were excluded. In addition to these selection criteria, we imposed $-1.0 \leq B - V \leq 3.0$ and $-1.0 \leq V - I \leq 4.0$ as colour constraints.

The reliability of the angular clustering measures implies a uniform correction of photometric zero-points between the observed fields. Table 5 shows the small variations associated with the $V - I$ colour, which span 0.03 and 0.07 mag. These values are consistent with the rms variations reported by McCracken et al. (2001) and Cabanac et al. (2000).

7.1. 2p-ACF estimator

The 2p-ACF, $\omega(\theta)$, gives the excess of probability, with respect to a random homogeneous distribution, of finding two galaxies in the solid angles $d\Omega_1$ and $d\Omega_2$ separated by an angle θ, and it is defined as

$$dP = \mathcal{N}^2 \, [1 + \omega(\theta)] \, d\Omega_1 d\Omega_2 \qquad (5)$$

where $\mathcal{N}$ is the mean number density of catalogued galaxies (Martínez & Saar 2002).

Beyond the formal definition, there are a handful of estimators to calculate $\omega(\theta)$ described in the literature (e.g. Peebles 1983; Hewett 1982; Landy & Szalay 1993; Hamilton 1993). In this work, we adopt the algorithm of Landy & Szalay (1993) to measure the 2p-ACF. Several authors argue convincingly that this estimator is preferable from a practical point of view (Kerscher et al. 2000; Pons-Bordería et al. 1999) due to its demonstrated advantages in the handling of intrinsic errors and border effects. Using the notation introduced by Roche & Eales (1999), the estimator has the form

$$\omega(\theta_i) = \frac{DD - 2DR + RR}{RR} \qquad (6)$$

where $DD = N_{\rm gg}(\theta_i)$ is the fraction of possible *galaxy-galaxy* pairs counted in i-bins over the angular range studied, and $DR = \left[\frac{(N_{\rm g}-1)}{2N_{\rm r}}\right] N_{\rm gr}(\theta_i)$, $RR = \left[\frac{N_{\rm g}(N_{\rm g}-1)}{N_{\rm r}(N_{\rm r}-1)}\right] N_{\rm rr}(\theta_i)$ are the normalized counts of *galaxy-random* and *random-random* pairs in these bins, respectively. To make the random catalogues we placed $(50 \times N_{\rm gal})$ random points (where $N_{\rm gal}$ is the number of galaxies by field in each estimation) but avoiding the masked areas due to saturated stars (and their spikes) in the observed fields, as well as the CCD gap of the mosaic. We measure $\omega(\theta_i)$ in i-logarithmic bins of width $\Delta(\log\ \theta) = 0.2$ on the angular scales $2.3 \leq \theta \leq 360.0$ arcsec. The formal error associated with the 2p-ACF measured on individual fields is the Poissonian estimate $\sigma^2_\omega = \frac{1+\omega(\theta_i)}{DD}$. This scheme provides a lower limit to the uncertainties, but taking our motivation and the angular scales involved in this case into account, Poisson errors are similar to those obtained from more refined techniques (Postman et al. 1998; Magliocchetti & Maddox 1999; Gandhi et al. 2007, and references therein).

When the data of small area galaxy surveys is used to estimate a correlation function, observed values in each bin are underestimated by an additive quantity known as the "integral

constraint" (IC), defined as the double integral of an assumed true $\omega(\theta)$ over the field area Ω (Peebles 1980), i.e.,

$$\mathrm{IC} = \frac{1}{\Omega^2} \int \int \omega(\theta)\, \mathrm{d}\Omega_1\, \mathrm{d}\Omega_2. \quad (7)$$

Consequently, an artificial reduction in the amplitude of the 2p-ACF is expected if the observed number density of galaxies on each frame is used to estimate the true mean density of galaxies at the magnitude limit chosen. Following Cabanac et al. (2000), the correction of this bias can be written as follows, using the random-random correlation and assuming $\omega(\theta) = A_\omega \theta^{-0.8}$:

$$C = \frac{\sum N_{\mathrm{rr}}(\theta)\, \theta^{-0.8}}{\sum N_{\mathrm{rr}}(\theta)}\,. \quad (8)$$

The C values and the amplitudes A_ω were obtained by fitting $A_\omega(\theta^{-0.8} - C)$ in each field using the Marquardt-Levenberg algorithm.

7.2. Combining 2p-ACF of fields

To increase the 2p-ACF signal and, at the same time, to attenuate the undesirable effects of the cosmic variance (regarding the small area over we have conducted the survey), we combined the discrete measures of the 2p-ACF on each individual field. For this, we adopted the scheme presented by Woods & Fahlman (1997, and reference therein) with a slight variation subject to our specific purpose. Accordingly, the weighted average of the 2p-ACF for angular bin is given by

$$\omega_{\mathrm{comb}}(\theta) = \frac{\sum \eta_j\, \omega_j(\theta)}{\sum \eta_j} \quad (9)$$

where the summations extend over fields $j = 1, 2, 3$, and the weight η_j depends on the galaxy number densities and the mean seeing (0.9, 1.0, and 1.1 arcsec of the fields 1, 2, and 3, respectively). In all cases, the final errors for each bin are given by the variance of the 2p-ACF estimates in each point. All the 2p-ACF results reported in the next sections refer to the $\omega_{\mathrm{comb}}(\theta)$ estimations.

7.3. Star dilution

For the objects with $I > 21$, we have established a scheme of correction for star dilution similar to the one by Cabanac et al. (2000, and references therein), consisting of the application of a factor defined by

$$D_{\mathrm{star}} = \left(\frac{\hat{N}_{\mathrm{gal}}}{\hat{N}_{\mathrm{gal}} - N_{\mathrm{star}}} \right)^2 \quad (10)$$

where $\hat{N}_{\mathrm{gal}}$ is the average number of galaxies for interval of magnitude used in the calculation of the 2p-ACF and N_{star} the number of stars in this interval predicted by the Besançon model for stellar population synthesis of the Galaxy (Robin et al. 2003). The star-dilution corrections for interval of I magnitude are given in Col. 6 of Table 7. Due to the dependence of the model on a random field, each tabulated value is the arithmetic mean of 5 stellar count runs.

7.4. Modelling the 2p-ACF

Our clustering measurements as a function of limiting I magnitude and $V - I$ colour were compared to those made on the mock, semi-analytical, catalogues of Kitzbichler & White (2007). From these, we extracted 5 independent samples of galaxies with angular coverage corrected to our observed fields. The masks used for the 2p-ACF calculation with our data, as well as the colour and integral constraints, were also applied to the mock samples. Finally, the scheme above described for the ACF signal combination and error estimation was applied without changes to this data.

From the mock catalogues, we initially used the observer frame total apparent (AB) magnitude in the bands available. The AB magnitude was converted to the one established in this work using the expressions given in Frei & Gunn (1994).

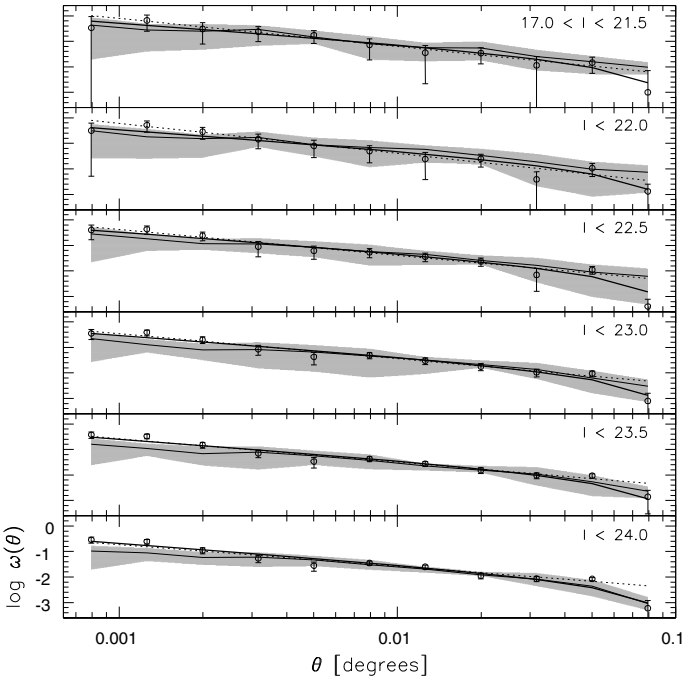

Fig. 8. 2p-ACF estimates as a function of I limiting magnitude. The continuous thick line represents the $A_\omega(\theta^{-0.8} - C)$ power law fit to the data (open circles), whereas the dotted line corresponds to the same but with A_ω and δ as free parameters. The 2p-ACF estimations based on mock catalogue data are represented by the continuous thin line. The shaded region is the envelope of errors associated with the latter.

7.5. The 2p-ACF as a function of I magnitude

First, we measured the 2p-ACF associated with the galaxies in each field individually as a function of limiting I magnitude in the intervals defined above, in order to give an estimate of the evolution of clustering and compare it with the model results and the findings in previous studies.

The measures were fitted using the $A_\omega(\theta^{-0.8} - C)$ and $A_\omega \theta^\delta$ power laws to perform a variance analysis of the errors and examine the behaviour of the amplitudes in the individual fields. Subsequently, we combined the measurements using the scheme described in Sect. 7.2. The results of this process are shown in Fig. 8, together with the power-law fits and 2p-ACF calculation from the mock catalogues of the Virgo-Millenium database. The parameters associated with the power-law fits corresponding to the *observed* (combined) and *model* catalogues are shown in Tables 7 and 8, respectively. The residuals between measured values, with respect to the $A_\omega(\theta^{-0.8} - C)$ power law fit and the results from the mock catalogues, are plotted in Fig. 9.

Table 7. Best-fit values of the power-law $\omega(\theta) = A_\omega\theta^\delta$ to the 2p-ACF of the observed galaxies as a function of I magnitude.

Interval I	Median I	$N_{\rm gal}$	A_ω $\times10^{-3}$	$-\delta$	A_ω ($\delta=-0.8$) $\times10^{-3}$	$\omega(1')$ $\times10^{-3}$	$D_{\rm star}$
17.0-21.5	20.81	988	0.39 ± 0.14	1.09 ± 0.20	2.10 ± 0.50	42.06 ± 9.92	1.15
17.0-22.0	21.29	1606	0.18 ± 0.18	1.17 ± 0.19	1.39 ± 0.30	27.78 ± 6.02	1.16
17.0-22.5	21.73	2507	0.38 ± 0.20	1.01 ± 0.12	1.34 ± 0.19	26.83 ± 3.84	1.10
17.0-23.0	22.18	3761	0.40 ± 0.11	0.98 ± 0.09	1.18 ± 0.12	23.68 ± 2.53	1.09
17.0-23.5	22.59	5404	0.46 ± 0.15	0.92 ± 0.07	1.02 ± 0.09	20.47 ± 1.74	1.07
17.0-24.0	22.94	7199	0.53 ± 0.16	0.85 ± 0.06	0.84 ± 0.06	16.89 ± 1.29	1.06

Note: The fitted values of A_ω ($\delta=-0.8$) and $\omega(1')$ with $\delta=-0.8$ are included. $D_{\rm star}$ is the corresponding estimate of star dilution.

Table 8. Best-fit values of the power-law $\omega(\theta) = A_\omega\theta^\delta$ to the 2p-ACF of the model galaxies from the mock catalogues of Kitzbichler & White (2007) as a function of I magnitude. As in Table 7, the fitted values of A_ω ($\delta=-0.8$) and $\omega(1')$ with $\delta=-0.8$ are included.

Interval I	Median I	$N_{\rm gal}$	A_ω $\times10^{-3}$	$-\delta$	A_ω ($\delta=-0.8$) $\times10^{-3}$	$\omega(1')$ $\times10^{-3}$
17.0-20.0	19.43	169	1.25 ± 0.15	1.13 ± 0.26	6.76 ± 2.98	135.34 ± 29.65
17.0-21.5	20.83	1169	1.33 ± 0.13	0.85 ± 0.12	2.11 ± 0.48	42.11 ± 9.72
17.0-22.0	21.29	1885	1.31 ± 0.22	0.78 ± 0.14	1.37 ± 0.30	27.41 ± 6.09
17.0-22.5	21.72	2894	1.27 ± 0.59	0.76 ± 0.13	1.17 ± 0.23	23.42 ± 4.60
17.0-23.0	22.17	4367	0.63 ± 0.30	0.83 ± 0.12	0.93 ± 0.18	18.52 ± 3.62
17.0-23.5	22.64	6492	0.38 ± 0.16	0.89 ± 0.09	0.78 ± 0.11	15.68 ± 2.28
17.0-24.0	23.11	9510	0.21 ± 0.09	0.94 ± 0.09	0.60 ± 0.09	12.04 ± 1.75

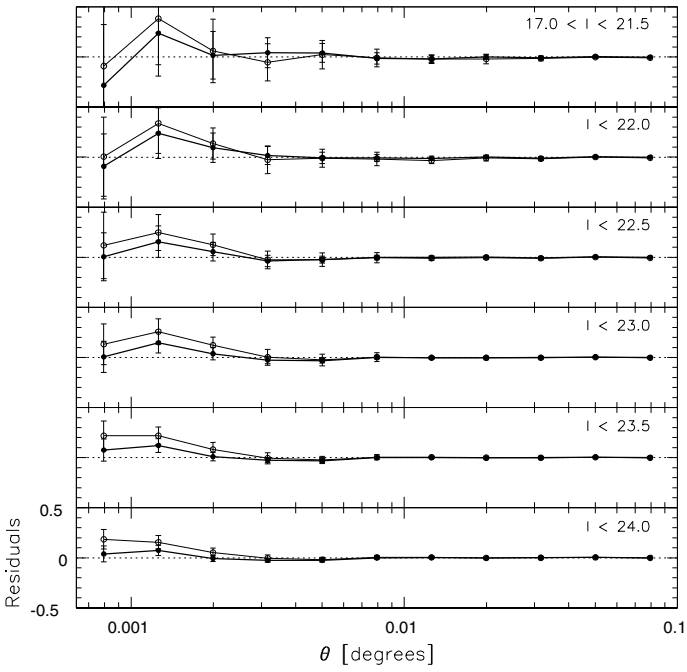

Fig. 9. Residuals of 2p-ACF estimates as a function of I limiting magnitude. The thick line represents the difference of measured values minus $A_\omega(\theta^{-0.8} - C)$ power-law fit. The thin line corresponds to the residuals between the former and the 2p-ACF measures obtained from the mock catalogues.

As expected, the amplitude of the correlation function decreases monotonically with increasing limiting magnitude. Analogously, a flattening of the slope, fitted δ (Table 7) with the limiting magnitude, is also evident.

On angular scales greater than ∼10 arcsec and for all magnitude ranges, the 2p-ACF successfully follows the $\delta = -0.8$ power law. Quantitatively, the significance level of Kolmogorov-Smirnov (K-S) statistics is better than 0.96 in this angular regime when the observed and model data are compared. The effect of the small area surveyed in our estimates is also clear. Likewise, the trend of the model-predicted signal demonstrates excellent agreement with the power-law fit of the observational data in all magnitude and scale ranges.

Below ∼10 arcsec and with $I_{\rm lim} \geq 22.5$, there is a marginally significant but systematic signal excess of the observed trend with respect to the fitted and model data (Fig. 9). We tried to isolate the origin of this effect by subtracting the red and blue subsamples of galaxies from our catalogue and recalculating the 2p-ACF. For instance, if the galaxies with $V - I \geq 2.00$ (or 2.25) colour are discarded, the maximal amplitude of the residuals on scales ≤10 arcsec diminishes around 55% (or 60%) and its statistical significance really disappears without perceptible changes in the general trend of the correlation function estimation. On the other hand, if we rule out the blue galaxies [$V - I \leq 0.8$] from the sample, the relative signal excess does not suffer appreciable changes. Consequently, one of the plausible sources of such effect on small scales in the surveyed area is the population of very red galaxies. Other possibilities are given in the literature: recent (deep) data seem to be suggesting an excess over the 2p-ACF $A_\omega\theta^{-0.8}$ power-law fit on scales below ∼11 arcsec (e.g. Ouchi et al. 2005; Lee et al. 2006) and the most common argument to explain it is related to the presence of multiple galaxies inside massive dark matter haloes (Grazian et al. 2006; Lee et al. 2006). The effect on the 2p-ACF estimation on such scales ($\lesssim$0.14 h^{-1} Mpc in redshift space) is consistent with a positive deviation with respect to the usual power law.

In Tables 7 and 8, the amplitude $\omega(\theta = 1$ arcmin) and the fitted parameters are given for the brightness ranges established. We compared our measurements with other works in a single plot, as shown in Fig. 10. Our values are corrected by star dilution. The results reported by Woods & Fahlman (1997) (up to $I \sim 25$), Cabanac et al. (2000) ($\sim 17 \leq I \leq 22.5$), and Coil et al. (2004) ($\sim 18 \leq I \leq 24$), as well as the values obtained from the model, are included in the plot.

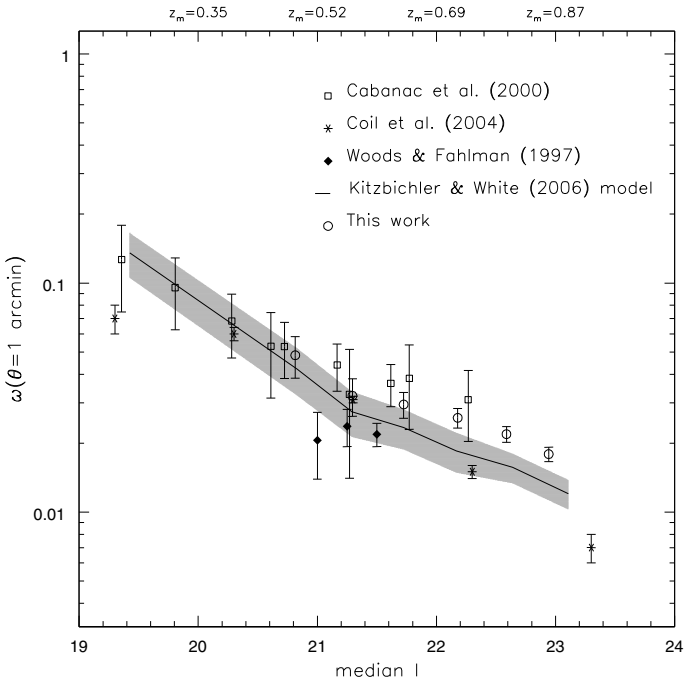

Fig. 10. Evolution of the 2p-ACF (δ = 1 arcmin). The plotted values associated with this work, which are given in Table 7, are corrected by star dilution. The continuous line connects the corresponding values from the mock catalogues given in Table 8. The shaded region is the envelope of errors associated with the latter. The median of the redshift (z_m) by I limiting magnitude on the top axis was calculated from the mock samples used in this work.

Our estimations track the general trend of the selected data from the literature, slightly favouring the Cabanac et al. (2000) values. Interestingly, the data from the model and its errors show fairly good agreement with the published values, specially with those that belong to this work. The significance level statistics (K-S) is 0.81 for a comparison between our data and model results.

Faintwards of $I \sim 22$, our data show a $\sim 2\sigma$ excess over the model amplitude. However, the values corresponding to the model tend to reproduce the flattening of the signal with the apparent magnitude seen in the observational data. This slope change is a natural prediction of N-body simulations in which there is a scale dependence to the growth of structures (Cabanac et al. 2000) and the model used here is not an exception. Even though there is other observational evidence of the flattening (Postman et al. 1998; Coil et al. 2004; Grazian et al. 2006), curiously there are some authors whose results do not show it (Woods & Fahlman 1997; McCracken et al. 2007). We return to this point in Sect. 8.

7.6. The 2p-ACF as a function of $V - I$ colour

In a similar procedure to the one used previously, we estimated the 2p-ACF for the observed and model galaxies as a function of the observed $V - I$ colour, with a limiting magnitude of $I = 24$. The results are given in Tables 9 and 10, respectively. In panel (a) of Fig. 11 the amplitude $\omega(\theta = 1$ arcmin) for both sets is represented as a function of the $V - I$ colour, whereas the residual of the observed with respect to the model signal is plotted in panel (b). We find that $\omega(\theta)$ strongly depends on the colour selected. Again, the significance level statistics (K-S) when data and model are compared in the range $0.0 \leq V - I \leq 3.2$ is about 0.83: the predicted trend traces the amplitude derived from our sample in this colour range remarkably well. In the case of the observed sample, the peak correlation amplitudes of the "very blue" and the "very red" subsamples (Fig. 11; the central part of this plot is referred hereafter as "intermediate colour" regime) differ only by a factor two, favouring the very red galaxy amplitude. Moreover, these peak amplitudes are about one order of magnitude higher than the $\omega(\theta = 1$ arcmin) value for whole galaxy population (which is represented by the average behaviour of the intermediate colour subsample).

The results obtained agree with those reported by Landy et al. (1996) (SA57 and SA68 regions, using $U - R_F$ colour, low-redshift population), Coil et al. (2004) (based on 5 fields, using $R - I$ colour) and McCracken et al. (2001) (based on 4 fields, using $V - I$ colour). In contrast, Brown et al. (2000) and Cabanac et al. (2000) report a weaker clustering of the blue galaxy sample against the red one for photometric surveys with a similar depth (also found by Coil et al. 2007, in their $z \sim 1$ sample), whereas Woods & Fahlman (1997) do not find any evidence of variations in clustering that are dependent on galaxy colour (based on 3 fields of faint galaxies, using $V - R$, $R - I$ and $V - I$ colours). In this case, we cannot find any reason that explains the clustering invariance with colour. On the other hand, the effects of the cosmic variance are naturally involved in the results cited,

Table 9. Power-law fits to $\omega(\theta) = A_\omega \theta^\delta$ for the combination of the 2p-ACF from the observed galaxies as a function of $V - I$ colour.

Interval $V-I$	Median $V-I$	N_{gal}	A_ω ($\delta = -0.8$) $\times 10^{-3}$	$\omega(1')$ $\times 10^{-3}$	D_{star}
–0.25–0.00	–0.09	71	11.68 ± 6.19	157.51 ± 30.31	1.00
0.00–0.25	0.14	145	5.70 ± 3.43	38.68 ± 29.10	1.02
0.25–0.50	0.39	298	1.44 ± 1.02	25.23 ± 8.58	1.02
0.50–0.75	0.64	576	1.51 ± 0.87	21.47 ± 7.22	1.10
0.75–1.00	0.88	858	1.43 ± 0.52	24.70 ± 3.23	1.09
1.00–1.25	1.13	1030	0.95 ± 0.42	19.14 ± 2.03	1.03
1.25–1.50	1.37	1027	0.73 ± 0.43	8.18 ± 0.94	1.03
1.50–1.75	1.62	803	1.18 ± 0.54	18.96 ± 5.81	1.04
1.75–2.00	1.87	665	1.63 ± 0.74	24.66 ± 3.69	1.05
2.00–2.25	2.11	491	3.20 ± 0.99	60.79 ± 6.33	1.04
2.25–2.50	2.37	371	4.41 ± 1.26	67.51 ± 9.22	1.03
2.50–2.75	2.61	280	4.79 ± 1.84	95.14 ± 13.36	1.07
2.75–3.00	2.86	177	6.24 ± 2.80	178.78 ± 11.92	1.11
3.00–3.25	3.11	112	10.32 ± 5.24	225.98 ± 35.74	1.18

Table 10. Power-law fits to $\omega(\theta) = A_\omega \theta^\delta$ for the combination of the 2p-ACF from the model galaxies as a function of $V - I$ colour.

Interval $V-I$	Median $V-I$	N_{gal}	A_ω ($\delta = -0.8$) $\times 10^{-3}$	$\omega(1')$ $\times 10^{-3}$
0.00–0.25	0.16	52	3.24 ± 1.26	64.59 ± 25.24
0.25–0.50	0.41	251	1.84 ± 0.62	36.68 ± 12.43
0.50–0.75	0.63	483	0.96 ± 0.35	19.05 ± 7.02
0.75–1.00	0.89	727	0.70 ± 0.26	13.88 ± 5.31
1.00–1.25	1.14	1117	0.45 ± 0.13	8.89 ± 4.71
1.25–1.50	1.39	1631	0.64 ± 0.21	12.82 ± 4.12
1.50–1.75	1.62	1679	0.85 ± 0.22	16.87 ± 4.34
1.75–2.00	1.86	1234	1.53 ± 0.50	30.55 ± 9.90
2.00–2.25	2.11	786	1.88 ± 0.38	37.58 ± 7.48
2.25–2.50	2.37	535	5.27 ± 0.72	105.21 ± 14.43
2.50–2.75	2.61	364	10.45 ± 1.79	208.43 ± 35.67
2.75–3.00	2.86	287	13.14 ± 2.75	261.94 ± 54.87
3.00–3.25	3.11	199	11.22 ± 2.53	223.76 ± 50.52

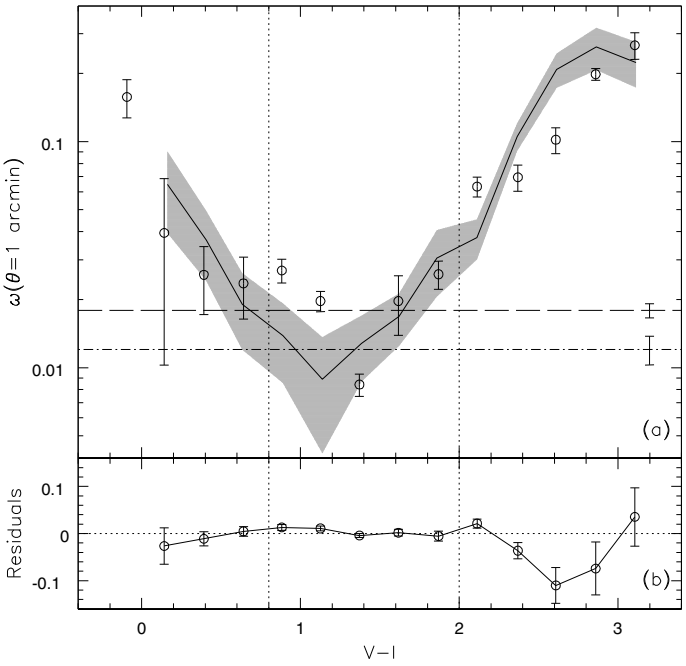

Fig. 11. Panel **a)**: 2p-ACF estimates as a function of the observed $V-I$ colour ($\delta = 1$ arcmin). The open circles represent the estimations of this work given in the Table 9, whereas the continuous line connects the corresponding estimations from the mock catalogues (Table 10). The shaded region is the envelope of errors associated with the latter. The dashed and dot-dashed lines represent A_ω ($\delta = -0.8$) for the observed and mock data, respectively, with $I_{\rm lim} = 24$. Panel **b)**: the continuous line represents the difference against the colour of observed minus model data estimations. The subtrahend of the residuals is the linear extrapolated value of the model estimation. The errors were added in quadrature. The plot is divided in the very blue, intermediate, and very red colour regions by vertical dotted lines.

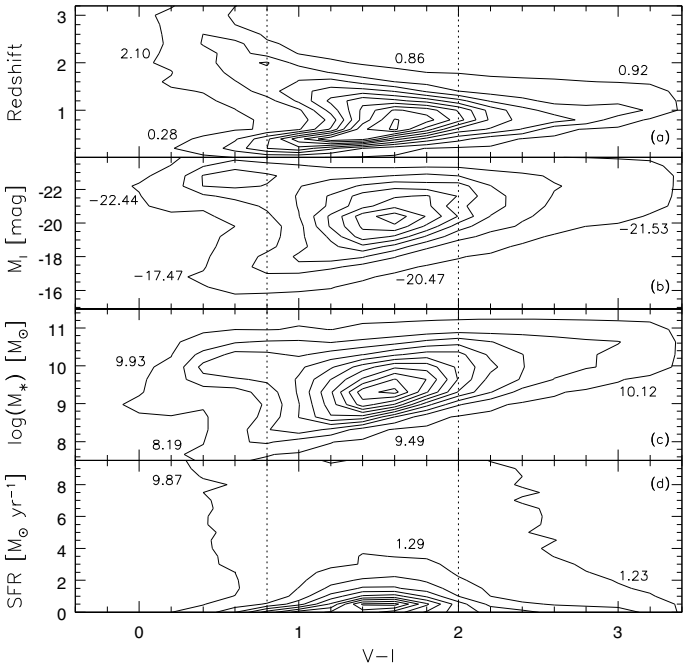

Fig. 12. Density distribution of mock galaxies in redshift, I-band absolute magnitude, stellar mass and SFR distributions against $V-I$ colour. The dashed lines separate the very blue, intermediate colour, and very red regimes, as in Fig. 11. Numbers inserted denote the median value of the corresponding variable in each colour interval except in the blue regime, where two populations (segregated by redshift) are evident in the first three plots. The step of density isocontours (in galaxies per rectangular cell of 0.2 mag in colour space) is 150, starting from 20.

including this work: Weiner et al. (2005) report the existence of "walls" and filaments due to a large-scale structure crossing the volume corresponding to the Groth strip, with the most prominent ones at $z = 0.28$, 0.81, and 0.99. Our surveyed area covers the DEEP survey region almost entirely. Consequently, a component of the clustering amplitude in the intermediate and very red colour regimes could be attributed to the large-scale structures present in the fields surveyed.

Given the similarity between the correlation amplitudes corresponding to the observed data and the model, it is tempting (at least as an exercise to understand the colour dependence of the 2p-ACF and to explain our results) to analyse the overall trend of some relevant galaxy properties included in the mock catalogues. In Fig. 12 the redshift, I-band absolute magnitude, stellar mass, and SFR distribution of the galaxies from the Kitzbichler & White (2007) mock samples used in this work are shown with respect to the observed $V-I$ colour. The "very blue", "intermediate colour" and "very red" colour subsamples represent 11%, 70%, and 19% of the entire sample, respectively.

In a general sense, a dependence of the colour (and the clustering amplitude) on the luminosity and the stellar mass is evident; as galaxies are more massive and luminous, they are more clustered. In addition, if the bulk of the SFR distribution (isodensities higher than 20) is considered, the well-known signature of the anticorrelation between the clustering and this variable is noticeable (Bongiovanni et al. 2005, and references therein).

It is obvious that the bluest subsample is distributed in two distinguishable populations. The "high-redshift" one (with $z > 1$ and a median value of $z = 2.10$) is 3.5 times more rich than the "low-redshift" set (with $z < 1$ and a median of $z = 0.28$). According with the clustering amplitude evolution, the low-z population contributes ~2.6 times more than the former to the clustering signal. This behavior repeats itself in the I luminosity and stellar mass distributions.

The high-z population of very blue galaxies is characterised by the highest I luminosity (median $M_I = -22.44$), mainly produced by high $SFR > 11\ M_\odot\ {\rm yr}^{-1}$, that is, almost 10 times above the median for the whole sample. Following Landy et al. (1996), these galaxies could correspond to a mixture of mergers and high-mass isolated galaxies with enhanced star formation episodes, in both cases precursors of normal galaxies at $z < 1$.

The low-z population of blue galaxies is marked by the lowest limits in luminosities and stellar masses, with mild SFR. It is not difficult to associate this subsample to a local blue galaxy population with surface brightness low enough to be undetectable in some extragalactic surveys.

In other words, if the mock sample is considered as an accurate representation of the observed one, the bluest trend of the clustering amplitude could be attributed to a superposition of the contributions from two different galaxy populations. The apparently divergent findings outlined at the beginning of this section can be explained if the galaxy detectability shows a colour dependency, or may just be a consequence of the cosmic statistics.

Finally, the very red population is spatially distributed in $0.3 \leq z \leq 1.8$, with a median value in $z = 0.92$ and exhibits the highest median of stellar mass ($\log M_* = 10.12$) and the lowest median SFR. This could be consistent with a population of early-type (E/S0) galaxies and, perhaps, the migration of blue galaxies that have experienced a cutoff in the star formation processes.

8. Summary

We have presented deep B, V, R, and I broad-band photometry of the Groth field, covering a total area of 0.18 sqr deg. The estimations of galaxy number counts are found similar to those obtained by others authors (McCracken et al. 2003; Metcalfe et al. 1995). Nevertheless, the analytical models cannot reproduce our values appropriately. From the semianalytic model application of Kitzbichler & White (2007), we extracted 9 mock catalogues to obtain estimates of number counts in the bands available. The agreement between this model and the observations is excellent in all bands.

We measured the two-point angular correlation function using the deep photometric data described in this work up to $I = 24$. Combining the individual estimations for the 3 observed fields, we obtained a galaxy clustering profile as a function of the limiting magnitude and the observed $V - I$ colour. The main results can be summarised as follows:

- We find evidence of clustering evolution. In a model-estimated redshift from $z \simeq 0.9$ to $z = 0.4$ the clustering amplitude increases by a factor of ∼5. Our data also favour a flattening of the clustering amplitude with median I. This is consistent with a dependence of the scale on the growth of spatial structures.
- We find a strong dependence of $\omega(\theta)$ on the observed $V - I$ colour. The very blue and very red galaxy populations show clustering peak amplitudes ∼10 times greater than the whole sample. The peak amplitude of the very red subsample is about 2 times greater than that of the very blue one.
- In both clustering approaches we find excellent agreement between our correlation function measurements and the estimates derived from the mock catalogues of Kitzbichler & White (2007). In the case of the colour dependence, this fact impelled us to explore the behaviour of I-band absolute magnitude, stellar mass, and SFR distributions of the model galaxies and find possible explanations for the observed results. We conclude that the correlation amplitude enhancement for the bluest subsample is probably caused by a mixture of a local, low stellar-mass and luminosity population (e.g. BCD galaxies), and a high-redshift, very luminous and vigorous star-forming one. The enhancement for the reddest population would essentially be due to galaxies distributed in the redshift interval $0.3 \leq z \leq 1.8$, with stellar masses above $10^9\ M_*\ h^{-1}$ and low SFR, likely to be E/S0 galaxies or their local counterparts.

Acknowledgements. This work was supported by the Spanish *Plan Nacional de Astronomía y Astrofísica* under grants AYA2005–04149 and AYA2006–2358. We thank the referee for helpful comments that improved the clarity of this paper. The Millennium Simulation databases used in this paper and the web application providing online access to them were constructed as part of the activities of the German Astrophysical Virtual Observatory.
IRAF is distributed by the National Optical Astronomy Observatory, which is operated by the Association of Universities for Research in Astronomy (AURA) under cooperative agreement with the National Science Foundation.
This publication makes use of data products from the Two Micron All Sky Survey, which is a joint project of the University of Massachusetts and the Infrared Processing and Analysis Center California Institute of Technology, funded by the National Aeronautics and Space Administration and the National Science Foundation.

References

Alfaro, E. J., Cepa, J., Gallego, J., et al. 2003, Rev. Mex. Astron. Astrofis., 16, 255
Arnouts, S., Cristiani, S., Moscardini, L., et al. 1999, MNRAS, 310, 540
Barmby, P., Alonso-Herrero, A., Donley, J. L., et al. 2006, ApJ, 642, 126
Bland-Hawthorn, J., & Jones, D. H. 1998, PASA, 15, 44
Benítez, N. 2000 ApJ, 536, 571
Bertin, E., & Arnouts, S. 1996, A&AS, 117, 393
Bolzonella, M., Miralles, J.-M., & Pelló, R. 2000, A&A, 363, 476
Bongiovanni, A., Bruzual, G., Magris, G., et al. 2005, MNRAS, 359, 930
Bosselli, A., & Gavazzi, G. 1994, A&A, 283, 12
Broadhurst, T. J., Ellis, R. S., & Glazebrook, K. 1992, Nature, 355, 55
Brown, M. J. I., Webster, R. L., & Boyle, B. J. 2000, MNRAS, 317, 782
Bruzual, A. G., & Charlot, S. 1993, ApJ, 405, 538
Cabanac, R. A., de Lapparent, V., & Hickson, P. 2000, A&A, 364, 349
Capak, P., Cowie, L. L., Hu, E. M., et al. 2004, ApJ, 127, 180
Cepa, J., Alfaro, E. J., Bland-Hawthorn, J., et al. 2003, Rev. Mex. Astron. Astrofis, 16, 64
Cepa, J., Aguiar, M., Castañeda, H. O., et al. 2005a, Rev. Mex. Astron. Astrofis, 24, 1
Cepa, J., Alfaro, E. J., Bland-Hawthorn, J., et al. 2005b, Rev. Mex. Astron. Astrofis, 24, 82
Cepa, J., Alfaro, E. J., Castañeda, H. O., et al. 2007, Rev. Mex. Astron. Astrofis, 29, 168
Coil, A. L., Newman, J. A., Kaiser, N., et al. 2004, ApJ, 617, 765
Coil, A. L., Newman, J. A., Croton, D., et al. 2007, [arXiv:astro-ph/0708.0004]
Colless, M., et al. 2001, MNRAS, 328, 1039
Coppin, K., Halpern, M., Scott, D., Borys, C., & Chapman, S. 2005, MNRAS, 357, 1022
Cristóbal-Hornillos, D., Balcells, M., et al. 2003, ApJ, 595, 71
Davis, M., et al. 2000, Proc. of the ESO/ECF/STSCI Workshop on Deep Fields (Springer)
De Lucia, G., Kauffmann, G., & White, S. D. M. 2004, MNRAS, 349, 1101
Eliche-Moral, M. C., Balcells, M., Prieto, M., et al. 2006, ApJ, 639, 644
Frei, Z., &, J. E. 1994, AJ, 108, 1476
Gandhi, P., Garcet, O, Disseau, L., et al. 2007, A&A, 999, 99
Gardner, J. P. 1998, PASP, 110, 291
Gardner, J. P., Sharples, R. M., Carrasco, B. E., & Frenk, C. S. 1996, MNRAS, 282, L1
Georgakakis, A., Nandra, K., Laird, E. S., et al. 2006, MNRAS, 371, 221
González-Serrano, I., Cepa, J., Pérez-García, A. M., et al. 2005a, Rev. Mex. Astron. Astrofis, 24, 247
González-Serrano, I., Cepa, J., Gallego, J., Cepa, J., Gallego, J., et al. 2005b, Rev. Mex. Astron. Astrofis, 24, 245
Gould, A., Bahcall, J. N., & Flynn, C. 1997, ApJ, 482, 913
Grazian, A., Fontana, A., Moscardini, L., et al. 2006, A&A, 453, 507
Hamilton, A. J. S. 1993, ApJ, 417, 19
Harris, W. E. 1990, PASP, 102, 949
Hewett, P. C. 1982, MNRAS, 201, 867
Hippelein, H., Maier, C., Meisenheimer, K., et al. 2003, A&A, 402, 65
Im, M., Simard, L., Faber, S. M., et al. 2002, ApJ, 571, 136
Jester, S., Schneider, D. P., Richards, G. T., et al. 2005, AJ, 130, 873
Jones, D. H., Shopbell, P. L., & Bland-Hawthorn, J. 2002, MNRAS, 329, 759
Jones, P. B. 1991, MNRAS, 253, 279
Kashikawa, N., Shimasaku, K., Yasuda, N., et al. 2004, PASJ, 56, 1011
Kerscher, M., Szapudi , I., & Szalay, A. S. 2000, ApJL, 535, 13
Kitzbichler, M. G., & White, S. D. M. 2007, MNRAS, 376, 2
Koo, D. C., Simard, L., Willmer, C. N. A., et al. 2005, ApJS, 157, 175
Kron, R. G. 1980, ApJS, 43, 305
Landy, S. D., & Szalay, A. S. 1993, ApJ, 412, 64
Landy, S. D., Szalay, A. S., & Koo, D. C. 1996, ApJ, 460, 94
Le Fèvre, O., Vettolani, G., Garilli, B., et al. 2005, A&A, 439, 845
Lee, K., Giavalisco, M., Gnedin, O. Y., et al. 2006, ApJ, 642, 63
Lemson, G., & Virgo Consortium, the, 2006, [arXiv:astro-ph/0608019]
Lilly, S. J., Cowie, L. L., & Gardner, J. P. 1991, ApJ, 369, 79
Magliocchetti, M., & Maddox, S. J. 1999, MNRAS, 306, 988
Martínez, V. J., & Saar, E. 2002, Statistics of the Galaxy Distribution (Chapman & Hall)
MacDonald, E. C., Allen, P., Dalton, G., et al. 2004, MNRAS, 352, 1255
McCracken, H. J., Le Fèvre, O., Brodwin, M., et al. 2001, A&A, 376, 756
McCracken, H. J., Bertin, E., Dantel-Fort, M., et al. 2003, A&A, 410, 17
McCracken, H. J., Peacock, J. A., Guzzo, L., et al. 2007, ApJS, 172, 314
Metcalfe, N., Shanks, T., Fong, R., & Roche, N. 1995, MNRAS, 237, 257
Metcalfe, N., Shanks, T., Campos, A., & MacCracken, H. J. 2001, MNRAS, 323, 795
Miyaji, T., Griffiths, R. E., Lumb, D., Sarajedini, V., & Siddiqui, H. 2003, Astron. Nachr., 324, 24
Moles, M., et al. 2007, A&A, submitted
Monet, D. G., Levine, S. E., Canzian, B., et al. 2003, AJ, 125, 984
Nandra, K., Laird, E. S., Adelberger, K., et al. 2005, MNRAS, 356, 568
Nakamura, O., Fukugita, M., Yasuda, N., et al. 2003, ApJ, 125, 1682

Norberg, P., Laird, E. S., Adelberger, K., et al. 2002, MNRAS, 332, 827
Ouchi, M., Hamana, T., Shimazaku, T., et al. 2005, ApJ, 635, L117
Peebles, P. J. E. 1980, The Large Scale Structure of the Universe (Princeton University Press)
Peebles, P. J. E. 1983, ApJ, 274, 1
Peletier, R. F., & Willner, S. P. 1992, AJ, 103, 1361
Peng, C. Y., Ho, L. C., Impey, C. D., & Rix, H.-W. 2002, AJ, 124, 266
Pilbratt, G. L. 2005, A&AS, 207, 3501
Pons-Bordería, M. J., Martínez, V. J., Stoyan, D., Stoyan, H., & Saar, E. 1999, ApJ, 523, 480
Postman, M., Lauer, T. D., Szapudi, I., & Oegerle, W. 1998, ApJ, 506, 33
Robin, A. C., Reylé, C., Derrière, S., & Picaud, S. 2003, A&A, 409, 523
Rocca-Volmerange, B., & Guiderdoni, B. 1990, MNRAS, 247, 166
Roche, N., & Eales, S. A. 1999, MNRAS, 307, 703
Sánchez-Portal, M., Pérez-García, A. M., Cepa, J., et al. 2005, Rev. Mex. Astron. Astrofis, 24, 271
Saracco, P., D'Odorico, S., Moorwood, A., et al. 1999, A&A, 349, 751
Sarajedini, V. L., Koo, D. C., Phillips, A. C., et al. 2006, ApJS, 166, 69
Simard, L., Koo, D. C., Phillips, A. C., et al. 2002, ApJS, 142, 1
pringer, V., et al. 1997, Nature, 435, 629
Skrustskie, M. F., Cutri, R. M., Stiening, R., et al. 2006, AJ, 131, 1163
Stevenson, C. C. 1994, MNRAS, 267, 904
Tinsley, B. M. 1980, ApJ, 241, 41
Vogt, N. P., Koo, D. C., Phillips, A. C., et al. 2005, ApJS, 159, 41
Williams, R. E., Blacker, B., Dickinson, M., et al. 1996, AJ, 112, 1335
Williams, R. E., Baum, S. A., Bergeron, L. E., et al. 1998, BAAS, 30, 1366
Weiner, B. J., Phillips, A. C., Faber, S. M., et al. 2005, ApJ, 620, 595
Willner, S. P., et al. 2006, AJ, 132, 2159
Wolf, C., Meisenheimer, K., Rix, H.-W., et al. 2003, A&A, 401, 73
Woods, D., & Fahlman, G. G. 1997, ApJ, 490, 11
Xilouris, E. M., Byun, Y. I., Kyfalis, N. D., Paleologou, E. V., & Papamastorakis, J. 1999, A&A, 344, 868
Yasuda, N., Fukugita, M., Narayanan, V. K., et al. 2001, ApJ, 122, 1104
York, D. G., Adelman, J., Anderson, J. E., Jr., et al. 2000, AJ, 120, 1579
Zehavi, I., Blanton, M. R., Frieman, J. A., et al. 2002, ApJ, 571, 172